Sea Ice Detection and Monitoring Using UK TDS-1 GNSS-R Data

A. Alonso-Arroyo, *Student Member, IEEE*, V. U. Zavorotny, *Fellow, IEEE*, and A. Camps, *Fellow, IEEE*

Abstract

A sea ice detection algorithm developed using UK TDS-1 Global Navigation Satellite Systems (GNSS)-Reflectometry (GNSS-R) data over the Arctic and Antarctic regions is presented. It is based on detecting the coherence of the received GNSS reflected waveform or Delay-Doppler Map (DDM). Over the open ocean the scattered signal has a diffusive, incoherent nature; it is described by the rough surface scattering model based on the Geometric optics and the Gaussian statistics for the ocean surface slopes. Over sea ice, and in particular newly formed sea ice, the scattering is mostly coherent which is typical for a mostly flat surface. In order to measure the degree of coherence of the received waveform or DDM three different estimators are presented: the normalized DDM average, the Trailing Edge Slope (TES), and the matched filter approach. Here we present a probabilistic study based on a Bayesian approach using two different and independent ground-truth datasets. This approach allow us thoroughly assessing the performance of the estimators. The best results are achieved for both the TES and the matched filter approach with a probability of detection of 97%, a probability of false alarm of $\sim$ 2%, and a probability of error of 2.5%. However, the matched filter approach is preferred due to its simplicity. The measurement of the sea ice concentration is also assessed in this work, but the nature of the UK TDS-1 data (lack of calibrated data) does not allow us to make any specific conclusions about the sea ice concentration.

Index Terms

Sea Ice, coherent scattering, incoherent scattering, GNSS-R, UK TDS-1

I. INTRODUCTION

Global warming represents a growing concern for the society due to the drastic consequences it may have on our planet. One of its consequences is the melting of the Antarctic ice and the consequent rise of the sea level, which is a serious threat for all cities located near the coastline. One source of information to analyze climate models and evaluate the effects of global warming is the sea ice extent parameter, which is the area on the Arctic and Antarctic regions covered by sea ice. The rise of temperature will reduce the area covered by sea ice year after year, which is an early warning of a forthcoming bigger problem: the polar ice caps melting.

Active and passive techniques have been used to monitor sea ice. Passive techniques based on microwave radiometry have been used to determine the Sea Ice Concentration (SIC) parameter, which is the percentage of ice on a pixel [1]. For instance 0% indicates open water, 50% indicates that half of the pixel is covered by ice, and 100% indicates that the whole pixel is solid ice. Active techniques based on real aperture radar and synthetic aperture radar generally measure surface roughness, which leads to sea ice type classification, as the

waveform shape is highly sensitive to surface roughness. However, in order to achieve a high resolution the frequency band used is normally Ku-band or K-band (12-18 GHz and 18-26 GHz respectively), which makes the radar technique sensitive to small ($\sim$ cm) and large ($\sim$ m) scale roughness.

The idea of using GNSS signals of opportunity for remote sensing purposes first was discussed in the late 80s [2]. One of its direct applications is the use GNSS reflected signals for mesoscale altimetry, as proposed in 1993 with the PAssive Reflectometry and Interferometry System (PARIS) concept [3]–[5]. It is a passive technique, as it uses the GNSS signals already transmitted by satellites for navigation purposes, and only a receiver is needed. In 2000, initial results comparing the waveform peak power of the GNSS reflected signals over ice against RADARSAT back-scattering echoes were presented [6]. In 2003, a theoretical model explaining the sea ice scattering was proposed [7]. In 2006, it was shown that there is a strong presence of the coherent component in the GNSS-R bistatic scattering echoes [8], indicating a deficiency of a purely diffusive scattering model. This was confirmed in 2010 with a detailed study using United Kingdom Disaster Monitoring Constellation (UK-DMC) GNSS-R dataset [9]. However, unambiguous relations between waveform peak power or shape and sea ice parameters have not been found. Airborne studies using GNSS-R data were also performed in 2010 for the determination of sea ice parameters. Also, the effect of surface roughness was analyzed and compared to lidar measurements [10].

In this work we propose and demonstrate the use of GNSS reflected signals for sea ice detection with simple and straightforward algorithms that can be implemented on future space-borne platforms. Section II shows the theoretical background that justifies the analysis performed along the entire work. Section III describes the approach followed based on the experimental evidence from UK TDS-1 mission. Section IV describes the ground-truth used to validate the analysis performed. Section V evaluates the GNSS-R approach against the available ground-truth. Section VI discusses the results achieved, the error sources, and the applicability of the techniques proposed. Finally, section VII presents the conclusions of this work.

II. THEORETICAL BACKGROUND

Conventional satellite radar altimetry was used for the sea ice studies long ago [11]. It relies on scattering of EM waves from the surface while the radar antenna is looking strictly at nadir. In that situation, the power waveform or returned power as a function of the delay is composed of three distinct components [11]–[13]:

$$W(\tau) = S_r(t) * P_{FS}(t) * r(t), \tag{1}$$

where $S_r(t)$ is the shape of the transmitted pulse or point target response, $P_{FS}(t)$ is the flat surface response, which is the radar cross-section as a function of the delay time (over the horizontal surface) weighted by the gain pattern, and $r(t)$ characterizes the surface roughness, and it is the mean density of point scatterers as a function of the delay time. In other words, $S_r(t)$ is a Doppler cut of the so-called Woodward Ambiguity Function (WAF) [14] through its maximum. $P_{FS}(t)$ depends on the antenna pattern and the radar cross-section, which at the same time depends on the probability density function of the surface's slopes. It determines the trailing-edge shape of the waveform while it affects also the leading-edge shape. Then, $r(t)$ characterizes generally the surface roughness parameter, and it is the main contributor to the leading-edge shape while it does not affect so severely the trailing-edge.

67 In the case of conventional GNSS-R (cGNSS-R) for the public C/A signal the equivalent radar pulse width is

68 approximately 300 meters (1 chip). This means that, unless there is a significant variation of surface topography,

69 Eqn. (1) can be approximated by Eqn. (2):

$$W(\tau) = S_r(t) * P_{FS}(t), \tag{2}$$

70 as the radar pulse width is much larger than the immediate *rms* elevations. Note that a nadir-looking geometry

71 is a particular case of the forward-scattering mechanism found in GNSS-R, and consequently, part of the

72 previous work done for altimetry can be used. In that direction, this waveform model is a particular case of

73 the waveform/DDM model proposed by Zavorotny and Voronovich in 2000 [15] for determining the shape of

74 the rough ocean scattered signals:

$$W(\tau, f_D) = T_c{}^2 \int \frac{|r(\vec{\rho})|^2 D^2(\vec{\rho}) \Lambda^2 \left(\tau - (R_r(\vec{\rho}) + R_t(\vec{\rho}))/c\right) q^4(\vec{\rho})}{4 R_r{}^2(\vec{\rho}) R_t{}^2(\vec{\rho}) q_z^4(\vec{\rho})} |S(f_D(\vec{\rho}) - f_c)|^2 P\left(-\frac{q_\perp(\vec{\rho})}{q_z(\vec{\rho})}\right) d^2\rho \tag{3}$$

75 where T_c stands for the coherent integration time, r for the Fresnel reflection coefficient, the WAF is approxi-

76 mated by a triangular function Λ in the time domain and by a sinc function S in the frequency domain, q stands

77 for the scattering vector, ρ is a vector from the specular reflection point to the scattering point, R_r is the distance

78 between the scattering point and the receiver, R_t is the distance between the transmitter and the scattering point,

79 q_z is the vertical component of the scattering vector, $q_\perp$ is the absolute value of the x,y components of the

80 scattering vector, and $P(\vec{v})$ is the probability density function (*pdf*) of the surface slopes. Note that this model

81 is based on the Kirchoff-Approximation Geometric-Optics (KA-GO), like Eqn. (1), and only takes into account

82 the non-coherent component, assuming that the coherent component is negligible. Equation (3) can be expressed

83 in a simplified form as in [16]–[18]:

$$W(\tau, f_D) \triangleq |\chi(\tau, f_D)|^2 ** |\sigma^0(\tau, f_D)|^2, \tag{4}$$

84 where f_D takes into account the power spreading in the Doppler domain, χ stands for the WAF, σ^0 for the

85 normalized bi-static radar cross section which includes already the antenna pattern projection over the surface,

86 the distance parameters, and the surface parameters such as the *pdf* of the surface slopes, and $**$ expresses a

87 convolution in both domains τ and f_D. Taking a cut over the Doppler domain, which results in the so-called

88 waveform, makes Eqn. (2) and (4) equivalent. In both altimetric and GNSS-R models, only surface scattering is

89 taken into account. However, in 2003 Wiehl et al. [7] proposed a model that takes into account the sub-surface

90 reflection that may occur on the ice sheets, converting Eqn. (4) into a triple convolution which can be expressed

91 as:

$$W_v(\tau, f_D) = Z(t) * W(t, f_D), \tag{5}$$

92 where Z models the subsurface scattering or the power echo from each different ice layer, and W is the DDM

93 model shown in Eqn. (4).

94 Although the theoretical models were proposed, no experimental cGNSS-R waveforms obtained from space

95 were available until 2005 with the launch of the UK-DMC satellite [8]. Therein, it is observed that the waveforms

96 reflected from the ocean surface and from the sea ice were significantly different. While over the ocean there
97 was a noticeable Delay-Doppler spreading of the signal power scattered leading to the "horseshoe" shape, the
98 DDM over the sea ice resembled the WAF itself, without a Delay-Doppler spreading. Furthermore, for several
99 regions the phase of the reflected signal at the DDM peak could be tracked, even identifying the navigation bits,
100 which indicates the presence of a strong coherent component [8]. This experimentally demonstrated that the
101 assumption of a negligible coherent component is mostly valid for the sea surface, but not for sea ice scattering.
102 In Fig. 2 of [19] this fact was conceptually illustrated for near-normal incidence angle, and the near-normal
103 incidence scattering cross section for the coherent and incoherent components were computed. Therein, it is
104 seen that the *pdf* of the slopes is much narrower for the sea ice than for the open sea, tending to a δ-function
105 centered at 0 for new ice, which means that the surface is perfectly flat and only coherent scattering occurs.
106 The transition to an almost flat surface cannot be done within Eqns. (3)-(5). The use of the slope probability
107 function in the form of a delta-function in these equations would lead to a wrong result. The coherent form of
108 the DDM should be based on the original Kirchhoff approximation for the scattered field under the assumption
109 that the surface roughness is very small (the Rayleigh parameter is significantly less than 1). The DDM model
110 for the coherent component was introduced in [20]. Instead of a convolution, as shown in Eqn. (4), it is a
111 product between the WAF and the surface reflectivity, times the factor that takes into account the loss of the
112 spatial coherence due to the presence of some relatively weak surface roughness (Rayleigh parameter) [21],
113 [22].

114   A deeper analysis of the sea ice signals scattered using the UK-DMC data was presented in [9], where
115 again the waveforms' shape indicated the presence of a coherent component. While the coherence seems to be
116 temporal with some fading, which means that the waveform peak value was quite constant with some fading
117 events, the coherent component dominates when the waveforms are incoherently summed . Therein, no clear
118 relations between waveform's observables and sea ice parameters were demonstrated in [9]. Furthermore, very
119 few public data were released from the UK-DMC mission, which reduces significantly the possibility of an open
120 data analysis, and it is one of the reasons why no specific conclusions could be made from the UK-DMC dataset
121 about the sea ice concentration, or other ice characteristics. The nature of the United Kingdom TechDemoSat-1
122 (UK TDS-1) data (lack of calibrated data) does not allow us to make any specific conclusions about the sea
123 ice concentration. Nevertheless, this space experiment provides a preliminary demonstration of the potential of
124 GNSS reflectometry over sea ice.

III. GNSS-R APPROACH

A. The "K-shape" DDM Concept

127   After analyzing several datasets from UK TDS-1 it has been seen that the shape of the measured DDM is
128 different depending on the surface the GNSS signal was reflected on. Figure 1 shows two different extracts of
129 the data retrieved from February 19th 2015 using the receiver specifications identification number RD000019,
130 and the tracklist identification number TD000071. Those two figures correspond to data from the northern
131 hemisphere (Arctic), and their spatial distance is below 60 km, as there is only 10 seconds difference among
132 their acquisition. In Fig. 1(a) it is possible to see, on the left, the DDM over a sea ice covered surface. Particularly,
133 the distribution of the power in the DDM resembles the shape of the letter "K" (rotated 90°). Therein, it is

possible to identify two different features. One of them is the vertical element of the "K" (horizontal line on the image), stretching along the Doppler frequency axis and depicting a partially-coherent DDM component. It corresponds to the WAF multiplied by the reflectivity, times second-order coherence function. The rest of the DDM, which spans over the Delay-Doppler domain with the "horseshoe" shape, corresponds to the incoherent component. For that particular DDM, that region has power levels similar to the WAF Doppler sidelobes, which are at least 13 dB below its maximum, indicating that the coherent component was the main scattering mechanism. On the right hand side of Fig. 1(a) the Doppler Integrated Waveform (DIW) in blue, a Doppler cut of the WAF in cyan, and a Doppler cut of the DDM in green are shown. The DIW is the integral of the DDM over the Doppler domain. This is a way to see the power spreading due to surface roughness but only in one dimension (the Delay domain). Without doing that, the spreading of the power over the delay domain is barely noticeable, as can be seen on the Doppler cut shown in the same figure in green. In Fig. 1(a) it is possible to see that the leading edge is not affected by surface roughness due to the large pulse width of the GNSS signals and the low roughness conditions. Also, due to the integral over the delay domain, the thermal noise below the leading-edge is averaged and reduced, showing the incoherent scattered power that could be barely seen on the conventional waveform (green)[1]. On the contrary, Fig. 1(b) shows a totally different effect. Therein, only the "horseshoe" shape of the DDM is seen and the WAF Doppler sidelobes are not present anymore. Also, even though the "horseshoe" shape of the DDM is an indicator of the surface roughness, the shape of the waveform's leading-edge is barely affected. Differently, the trailing-edge of the DIW is very different. In Fig. 1a there are two different regions on the trailing-edge, one where the slope is very large and follows the WAF shape (associated to the coherent component), and one where the slope is smoother and corresponds to the incoherent power. In Fig. 1(b) there is only one smooth region that can be identified which indicates the lack of coherent power, as there is no power drop after the WAF Delay decay.

These indicates two different scattering mechanisms that affect the scattering over sea ice or open water. When the reflection is purely coherent, there is no Delay-Doppler spreading and the reflected waveform is the WAF multiplied by the power Fresnel reflection coefficient. If the reflection is purely incoherent, there is a large Delay-Doppler spreading. The spreading depends on the roughness and in particular on the *pdf* of the slopes. It might be logical that when the reflection has a coherent part and a non-coherent part, the waveform is a linear combination of both models, as shown in Fig. 1(a). The more coherent, the more it will tend to the coherent model, and the more incoherent, the more it will tend to the model in [15]. The combination of both models tends to the "K-shape" DDM model. Furthermore, an inversely-proportional relationship was observed between these two components: the larger the coherent component, the smaller the incoherent one, and vice versa.

It has been theoretically [15] and empirically [8], [23] demonstrated that under open ocean conditions, even at weak winds, the surface will be rough, and the coherent component will be negligible [15]. On the other hand, there is no correct theoretical model that matches the waveforms obtained from the sea ice. The

---

[1]The Doppler domain integration of the DDM is only needed sometimes for GNSS-R spaceborne data, as due to the geometry and the platform's relatively high speed, the power is spread largely on the Doppler domain. Note that the Global Positioning System (GPS) satellite effective speed is much smaller than the platform's effective speed. For the airborne case, as the platform's speed is much lower, the Doppler spreading is not as large as the spaceborne case, and the waveform shows all the sensitivity to surface roughness on the trailing edge slope [15], without the need of a Doppler integral. Note that the slope of the DIW was proposed as an indicator of the ocean's *mss* [15].

coherent component can be introduced into the non-coherent model in two different ways. The first one, as aforementioned, could comprise of a bistatic radar equation (3) as a DDM incoherent part plus a separate DDM term which describes a coherent (or partially-coherent) component. The second one is to devise a single bistatic radar equation which would have, under the surface integral, a single combined bistatic radar cross section similar to that in [24]. The equivalent bistatic cross section will consist of a sum of two terms: one, the same as in Eq. (3) describing the incoherent diffuse scattering, and another, describing the coherent reflection from the flat component of the surface. Formally, this can be done, and previously this approach was used for simulating the coherent and incoherent received scattered power under the bistatic geometry for soil moisture monitoring purposes [25], [26]. However, it makes the combined bistatic radar cross section distance and antenna parameters dependent. It makes this approach at odds with a traditional definition of the radar cross section which should only be a surface dependent parameter.

B. Definition of the GNSS-R Observables

There are several approaches that have been used up to now in order to match simulated GNSS-R data with real data in order to retrieve the geophysical parameters. One of the most common is the waveform fitting [27]–[29], which consists of minimizing the cost function created using measured data and simulated one. This one has been widely used for the retrieval of wind-speed over the ocean. Other heuristic approaches have been used in order to infer the surface roughness, such as the Volume under the normalized DDM (V_{DDM}), or the area under the normalized waveform (A_{WF}) [30]. Furthermore, different heuristic approaches have been compared against the wind-speed over the ocean such as the DDM Average (DDMA), the DDM Variance (DDMV), the Allan DDM Variance (ADDMV), the Leading Edge Slope (LES), and the Trailing Edge Slope (TES) [31]. In [30] it was already stated the correlation between the (V_{DDM}), which can be seen as the DDMA for large a Delay-Doppler region, and the TES was 0.74.

UK TDS-1 data are DDMs time-referenced and geo-located with a coherent integration time of 1 ms and an incoherent integration time of 1 s. In other words, there is no access to the 1 ms complex DDMs generated in the operation to obtain the 1 s incoherently integrated DDM. The delay bin is approximately 244 ns, and the Doppler bin is 500 Hz. Consequently, any operation that can be done among 1 ms coherently integrated complex DDMs, such as the DDMV or the ADDMV must be discarded. Furthermore, data from UK TDS-1 is not calibrated, as there is no information about the direct signal power impinging on the ground or about the signal power at satellite level. This excludes the use of parameters such as the Signal-to-Noise Ratio (SNR), as there the transmitted power depends on the satellite used and is not constant along time. Consequently, all DDMs retrieved from UK TDS-1 have been normalized to its maximum. So, the CYclone Global Navigation Satellite System (CYGNSS) approach to the wind-speed retrieval based on the signal power received cannot be applied to UK TDS-1 data.

The lack of a theoretical model for sea ice surface forward scattering at L-Band prevails us from applying the cost function approach. However, initially we will focus on detecting the coherency level of the scattered signal for determining the sea ice presence, so a comparison with the full coherent scattering model can be performed. The following three heuristic approaches will be used, which basically measure the peakedness of the WAF or its similarity to the coherent model:

1) DDMA: it is the average value of the normalized DDM around its peak. For this analysis we have selected 3 different regions on the DDM.

- 3x3: 3 Doppler bin cells x 3 Delay bin cells
- 3x5: 3 Doppler bin cells x 5 Delay bin cells
- 3x7: 3 Doppler bin cells x 7 Delay bin cells

2) TES: it is the slope computed between the maximum of the normalized DIW and its value at different delay bins. For this analysis we have selected 3 different versions.

- 3-bin: approximately 750 ns after the peak power.
- 6-bin: approximately 1.5 μs after the peak power.
- 9-bin: approximately 2.25 μs after the peak power.

3) Matched Filter (MF): also understood as correlation approach, it computes how similar are the unitary energy DIW waveform is to the unitary energy WAF Doppler cut for the same satellite. It is an indirect measurement of how coherent is the reflection process.

The results obtained with the LES estimator, were not satisfactory and are not present in this work. One of the reasons is that at L-Band, as aforementioned, the waveform's leading edge is not as sensitive to surface roughness as it is at higher frequency bands, such as Ku-band, or K-band, which are the frequency bands of conventional altimeters, which also have much larger bandwidths. Furthermore, the higher the frequency used, the more sensitive it is to small scale roughness [32].

Similar observables for sea ice detection and classification have been used in conventional altimetry such as the SIGPK, which is the peak backscatter power in the returned echo, and the SIGTD, which is the average power computed between eight early and eight late delay bins of the DIW [33]. Note, that the SIGTD is similar to the DDMA approach and it is a measurement of the signal/waveform peakedness, or how much coherent is the echo returned. Also note that the SIGPK cannot be used with UK TDS-1 data due to the lack of calibrated data.
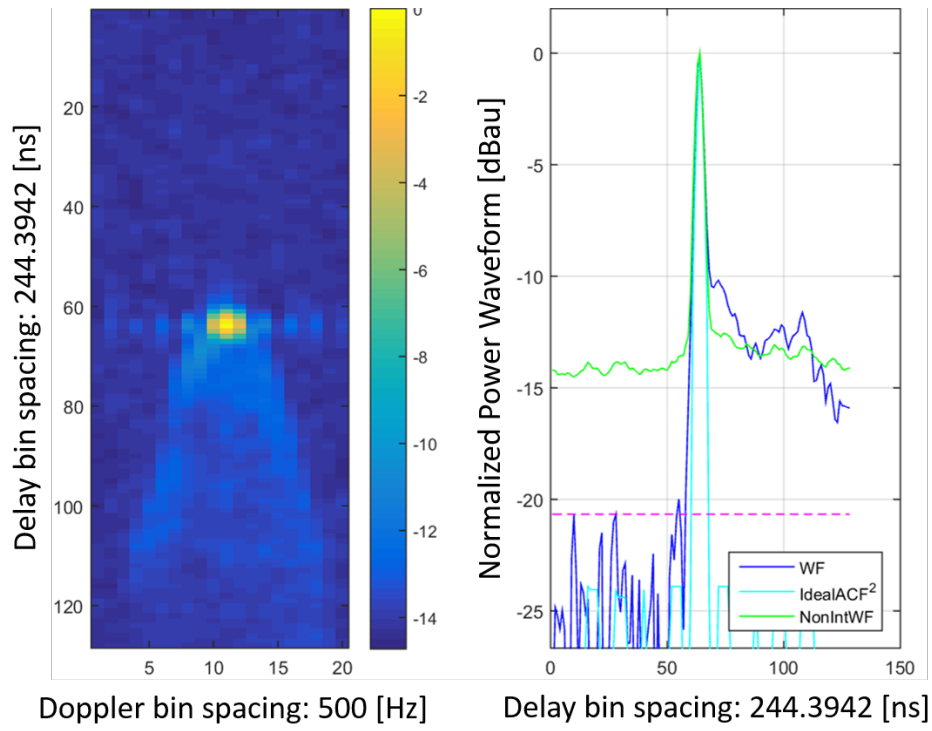
(a)
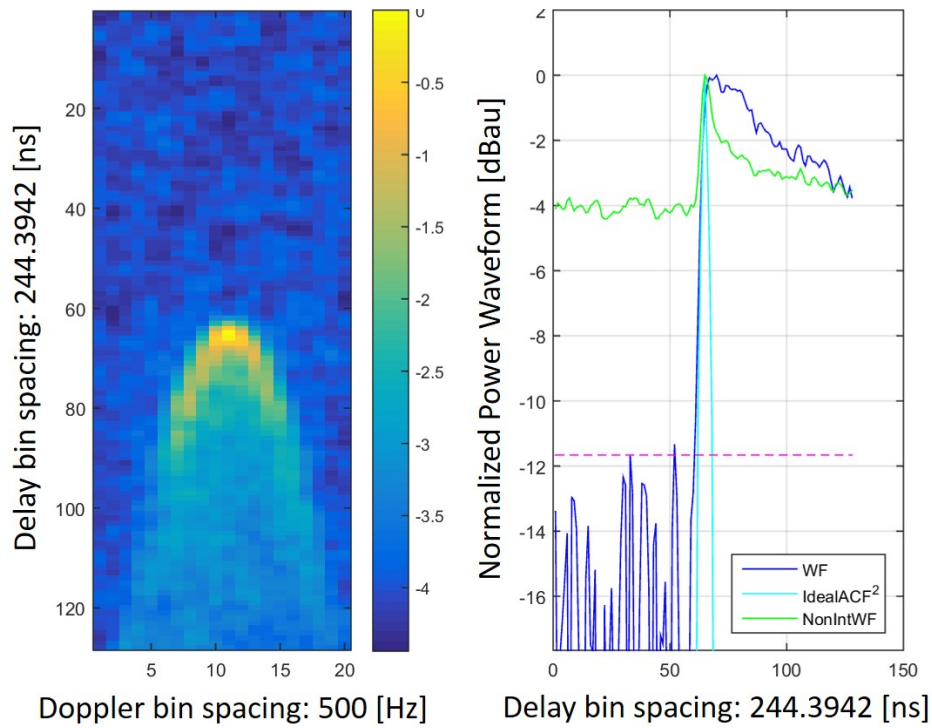
(b)

Fig. 1: Two DDMs and the corresponding waveforms for (a) sea ice and (b) open water regions.

IV. GROUND-TRUTH DESCRIPTION

In order to detect the presence of sea ice and compare it to the GNSS-R waveform shape, two different ground-truth SIC datasets have been used. The first one is the Arctic Radiation and Turbulence Interaction STudy (ARTIST) Sea Ice (ASI) [1] algorithm using AMSR2 data. The second one is the Ocean and Sea Ice SAF (OSISAF) [34] which is computed using data from the different channels of the SSMIS sensor.

A. ASI Algorithm using AMSR2 Data

The ASI algorithm was originally developed to use the high resolution provided by the 85 GHz channel of the SSM/I sensor. Herein, it is applied to the AMSR2 data, which was launched on May 18th 2012. The AMSR2 is a multi-frequency microwave radiometer with channels at 6.93, 7.3, 10.65, 18.7 23.8, 36.5, and 89 GHz. The SIC is calculated from the polarization difference of the 89 GHz channel. The ASI algorithm is based on the polarization difference of the H and V channels ($P = T_{BV} - T_{BH}$). At 89 GHz the polarization difference for all types of ice is very small, either first-year, multi-year, or pure ice, whereas for open water it is much larger. By measuring this polarization difference, the presence of ice is determined. The SIC is determined by a linear model, which decomposes the polarization difference in the contribution from open water, and the contribution of sea ice. Both of them are multiplied by a term that depends on the SIC. The lower the polarization difference, the larger the SIC and vice versa. Using this model a third degree polynomial is finally fitted to obtain the SIC as a function of the polarization difference. However, the 89 GHz frequency band is highly prone to atmospheric effects. Even though they have a poorer resolution, the lower frequency channels of the AMSR2 data are used to assess the quality of the retrievals obtained from the 89 GHz channel, taking into account atmospheric effects and discard data without a sufficient quality. The SIC maps[2] used as a ground-truth for the analysis developed along this work are obtained from [35]. For more information about the ASI algorithm the interested can refer to [1].

B. OSI SAF Data

The OSISAF algorithm is based on the combination of the data provided by the different channels of the SSMIS radiometer, in particular the 19 GHz, the 37 GHz, and the 91 GHz. The combination is generally performed using a Bayesian approach. Generally, the 91 GHz channel provides the high resolution (12.5 km x 12.5 km), and the other channels are used to compensate atmospheric factors as was done with the AMSR2 data. The retrieval algorithm is also based on the polarization difference between the V and H channels. However, in this algorithm the other channels are used in the model, and not only for quality assessment, resulting in a smoother transition between the open water and SIC larger than 80%. The SIC maps[3] used as a ground-truth for the analysis developed along this work are obtained from [36]. The OSISAF dataset provides other information apart from the SIC maps, such as the sea ice edge, and the the ice type. In order to develop those products also data from ASCAT scatterometer is used.

---

[2]Those maps are given in the polar stereographic coordinates for both hemispheres (Northern and Southern) using a grid resolution of 6.25 km. This implies that the GNSS-R data is converted into those coordinates in order to make the appropriate comparisons.

[3]Same than previous maps using a grid resolution of 10 km.

V. Sea Ice Monitoring using UK TDS-1 data

As experimentally seen, the coherency level on the GNSS-R waveform is an indicator of the sea ice presence. In order to assess the performance of the proposed estimators, which basically measure the coherency level of the GNSS-R waveform, some intermediate steps have been performed to the GNSS-R data. First of all, all available UK TDS-1 data with a latitude larger than 50° for the Northern hemisphere, and lower than -50° for the Southern hemisphere were downloaded. For that dataset, only those DDMs with a thermal SNR larger than 0 dB were used, as lower SNR indicates that the DDMs do not have a good quality. In previous analysis of UK TDS-1 data this parameter was even more restrictive (3 dB minimum SNR required) [37]. However, as UK TDS-1 orbit and GPS constellation were not designed to monitor polar areas, it is decided to lower this constrain as otherwise the dataset becomes very limited.

Regarding the ground-truth, the data has been split in Arctic and Antarctic regions, and the two different ground-truth datasets used, which leads to four different analysis. Also, a pixel has been considered as an ice pixel if the SIC value is larger than 5%. The pixel correspondence between the GNSS-R data and the ground-truth has been performed by a minimum distance algorithm between the geo-located GNSS-R data and the ground-truth grid. A landmask was applied to avoid land contaminated pixels on the data analysis.

A. Performance Evaluation of the Estimators proposed

Taking into account the previous assumptions, the sea ice detection performance for the different proposed estimators has been evaluated through a Bayesian approach. The *pdf* of the ice pixels and the open water pixel were computed and the threshold to determine the presence of ice was chosen using a maximum likelihood criterion, assuming no a priori information about the pixels content [38]. This means that the probability of having an ice pixel or an open water pixel, in the whole dataset, is assumed to be equal. Figure 2 shows the *pdf* of the estimators proposed for the Northern hemisphere using the AMSR2 dataset as ground-truth. Figures 2(a)-(c) show the performance of the DDMA algorithm for the three different approaches selected, using 3 Doppler bins and 3, 5, and 7 Delay bins. As it can be seen, the three of them look like very equal, and as the delay bins used increase, the threshold decreases. What occurs with this algorithm is that the smaller the area computed, the more similar to the WAF the reflected signal is. If the reflection is incoherent, then the reflected signal does not drop so quickly and the normalized DDMA increases. Figures 2(d)-(f) show the performance of the TES algorithm. In this case, the sharper the slope, the more more similar to the Doppler cut of the WAF the DIW is. Consequently, ice values appear on the right whereas with the DDMA they appeared on the left. Qualitatively, this estimator seems to perform better than the DDMA in each of its three different versions. Finally, the matched filter approach is shown in Fig. 2(g). Herein, it is possible to see that the *pdf* looks narrower and sharper than with previous estimators. Qualitatively, it seems to be the best estimator to distinguish between sea ice or open water.

The same operation has been performed for the OSISAF dataset, and for both ground-truth over the Antarctic region. The *pdf*s obtained are similar to the ones shown in Fig. 2, showing a similar behavior, which shows that the algorithms performed in the same way independently from the data nature. In order to summarize the results obtained and evaluate quantitatively the performance of all the estimators proposed, Tab. I is shown. Therein, four parameters are computed for each ground-truth available (OSISAF and ASI AMSR2), and each region
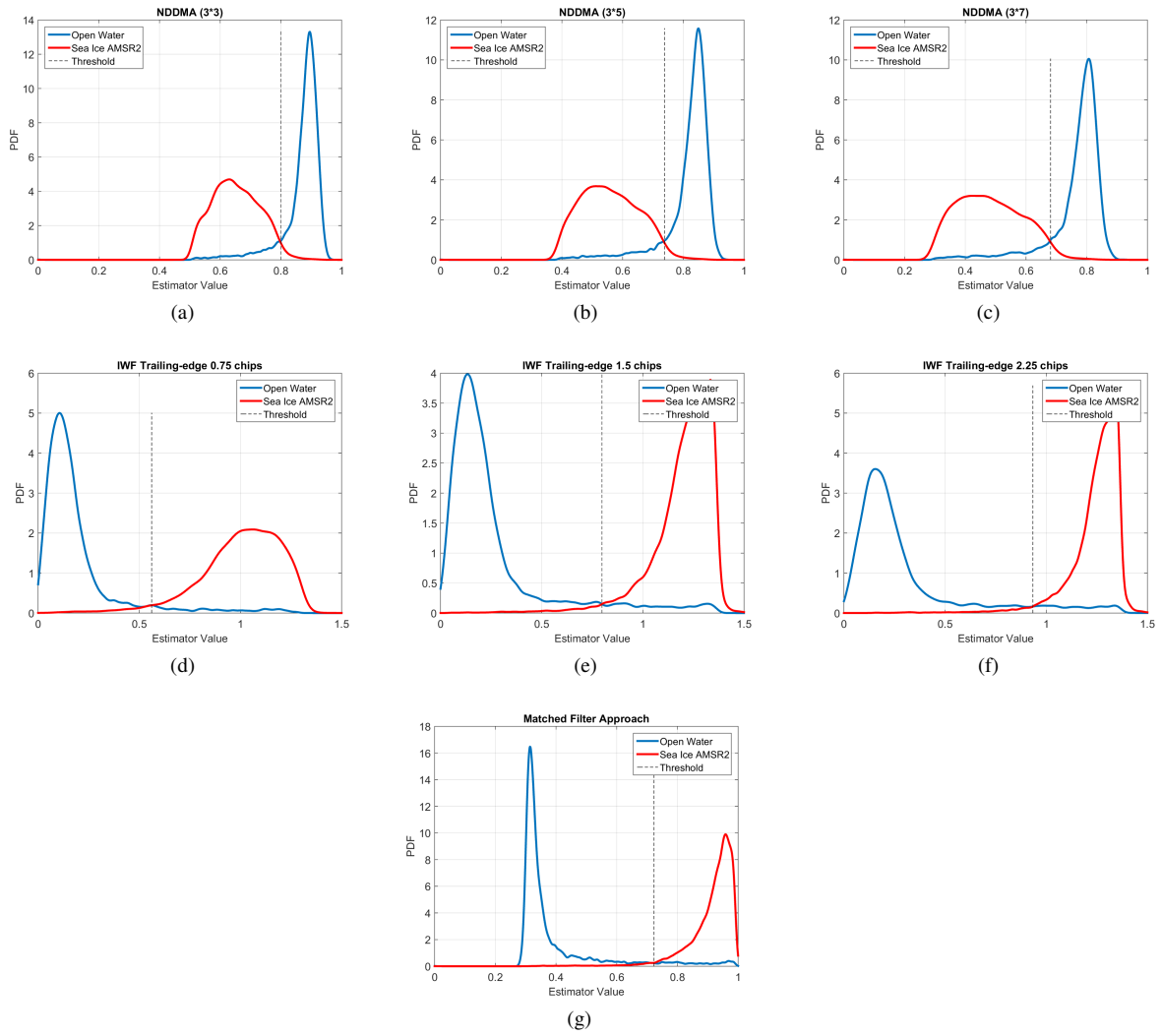
Fig. 2: Estimators performance for the Northern hemisphere using the AMSR2 dataset. (a) Normalized DDMA 3x3, (b) Normalized DDMA 3x5, (c) Normalized DDMA 3x7, (d) TES 750 ns, (e) TES 1.5μs, (f) TES 2.25μs, (g) Matched Filter.

(Arctic and Antarctic): the probability of detection (Pd), the probability of false alarm (Pfa), the probability of error (Pe), and the threshold selected [38].

In general, it is possible to see that, independently from the algorithm used, for any region and any ground-truth dataset, the Pd is larger than 95%, reaching larger values for the ASI AMSR2 ground-truth. However, for that dataset, the Pfa is also larger. In the end, there is always a compromise between the Pd and Pfa, and consequently, the larger the probability of detection, the larger the probability of false alarm. Note that the estimators with the worst performance, which is evaluated by the probability of error, are the ones based on the DDMA. However, those ones are consistent and independent from the ground-truth and the region observed, as they all have a similar threshold. This occurs because the threshold is determined by the shape of the *pdf*s, and for those estimators they are closer and the slopes around the threshold are larger. On the other hand, the threshold for the other estimators is not as consistent. Looking to the *pdf*s presented on Fig. 2, they are

more separated than for the DDMA, and the slopes around the threshold are smaller. This means that, the threshold selection is not so important, and the Pd and Pfa values will not change a lot by moving the threshold computed. Also note that the performance of the trailing edge estimators and the matched filter approach is similar. However, the matched filter approach seems to be less sensitive to the threshold selection just by qualitatively explore the *pdf*s. Furthermore, the matched filter approach is the simplest one to be implemented as it only requires one Fast Fourier Transform (FFT) and one Inverse FFT (IFFT). For this reason, it is the approach preferred, as it can be easily implemented in a real-time processing software on-board the satellite, without the need of further algorithm intelligence. Finally, it is also remarkable that the results obtained using the OSISAF dataset as ground-truth are better than the ones using the ASI algorithm over AMSR2 data. The reason for that is that the first ground-truth uses a combination of different frequency bands, detecting features that are not detectable at close to 90 GHz, which is the unique frequency band used by the ASI algorithm.

TABLE I: Performance evaluation of the estimators proposed for Arctic and Antarctic regions as a function of the two different ground-truths used, the OSISAF dataset, and the ASI AMSR2 dataset.

	Estimators	Arctic				Antarctic			
		Pd	Pfa	Pe	Th.	Pd	Pfa	Pe	Th.
OSISAF	NDDMA (3*3)	0.9650	0.0308	0.0325	0.808	0.9499	0.0596	0.0544	0.816
	NDDMA (3*5)	0.9615	0.0346	0.0361	0.745	0.9481	0.0620	0.0566	0.756
	NDDMA (3*7)	0.9564	0.0407	0.0417	0.686	0.943	0.0630	0.0597	0.694
	TE (0.75 CA Chips)	0.9668	0.0189	0.026	0.416	0.9528	0.0460	0.0465	0.342
	TE (1.5 CA Chips)	0.9718	0.0212	0.0247	0.619	0.9642	0.0520	0.0439	0.466
	TE (2.25 CA Chips)	0.9723	0.0209	0.0242	0.753	0.9629	0.0496	0.0433	0.597
	MF	0.9740	0.0234	0.0247	0.583	0.9628	0.0536	0.0453	0.510
ASI AMSR2	NDDMA (3*3)	0.9735	0.1014	0.0634	0.800	0.9703	0.1425	0.0856	0.806
	NDDMA (3*5)	0.9732	0.1038	0.0648	0.738	0.9699	0.1415	0.0854	0.741
	NDDMA (3*7)	0.9697	0.1111	0.0702	0.681	0.9700	0.1467	0.0880	0.685
	TE (0.75 CA Chips)	0.9666	0.0600	0.049	0.561	0.9676	0.1281	0.0760	0.413
	TE (1.5 CA Chips)	0.9728	0.0697	0.0484	0.798	0.9765	0.1273	0.0754	0.661
	TE (2.25 CA Chips)	0.9709	0.0710	0.0500	0.934	0.978	0.1292	0.0756	0.768
	MF	0.9721	0.0671	0.0474	0.723	0.9731	0.1233	0.0750	0.627

B. SIC Maps from Ground-truth and GNSS-R data

Figure 3 shows the sea ice detection maps created from the GNSS-R data using the matched filter approach together with the SIC maps from the two ground-truths available for both the Arctic and Antarctic regions. Note that February 15th is the middle of the winter in the northern hemisphere, and the middle of the summer in the southern hemisphere, which is why the whole north pole has plenty of sea ice whereas the south pole has very few. In all maps, the presence of ice is determined by the purple color whereas the presence of open water is determined by the light blue color, which corresponds to the colorbar on the right of the figures. The gaps are due to data with thermal SNR lower than 0 dB or land contaminated pixels. In the same way, the SIC from OSISAF and ASI AMSR2 are scaled from 0% to 100%, with the 0% to the dark blue and the 100% to the dark red, which corresponds to the colorbar on the left of the figures. The coordinate system used to represent those maps is the polar stereographic coordinate system. Therein, it is seen how the transitions between open water and sea ice are monitored, and the change observed is very drastic, as expected from the *pdf*s. The sea ice

edge is perfectly detected using the GNSS-R data. Based on specular reflection theory, for the sea ice regions assuming coherent reflection, and using the TDS-1 satellite parameters, the spatial resolution is $\sim$ 6 km x 0.4 km, which is half of the SSMIS pixel in the along-track track direction.

Furthermore, note that GNSS-R data look like different transects. This is one of the properties of the multi-static GNSS-R techniques. Instead of being an image like a Synthetic Aperture Radar (SAR) or a microwave radiometer, it is a collection of transects with all the satellites in view. In order to generate a map with GNSS-R data interpolation is required. Herein, the interpolation approach has not been performed as the mission specifications do not allow to obtain sufficient points to generate a reliable map. However, a GNSS-R mission with the appropriate specifications to monitor the polar regions such as the one simulated in [20] would provide enough quality data to generate polar images.
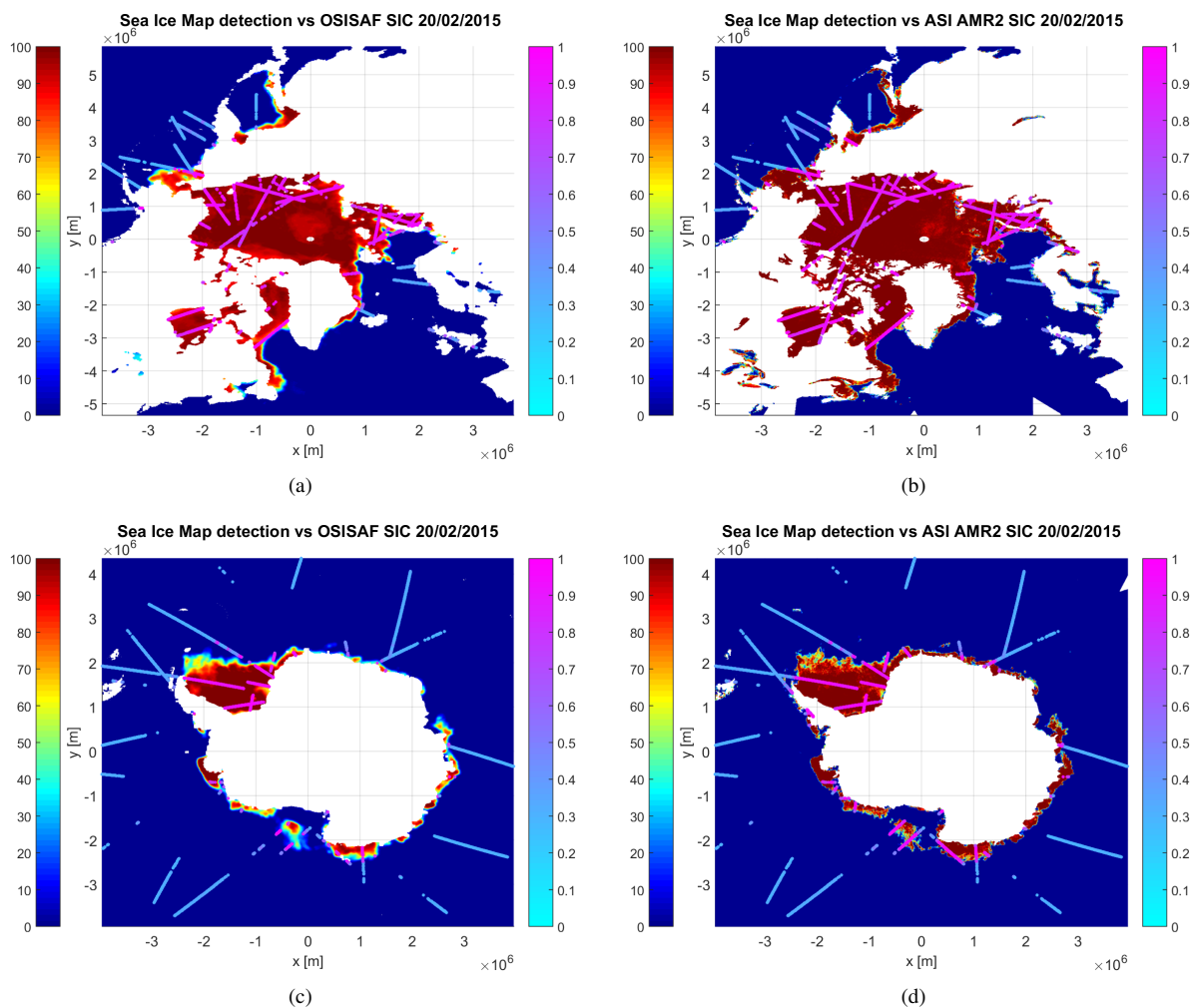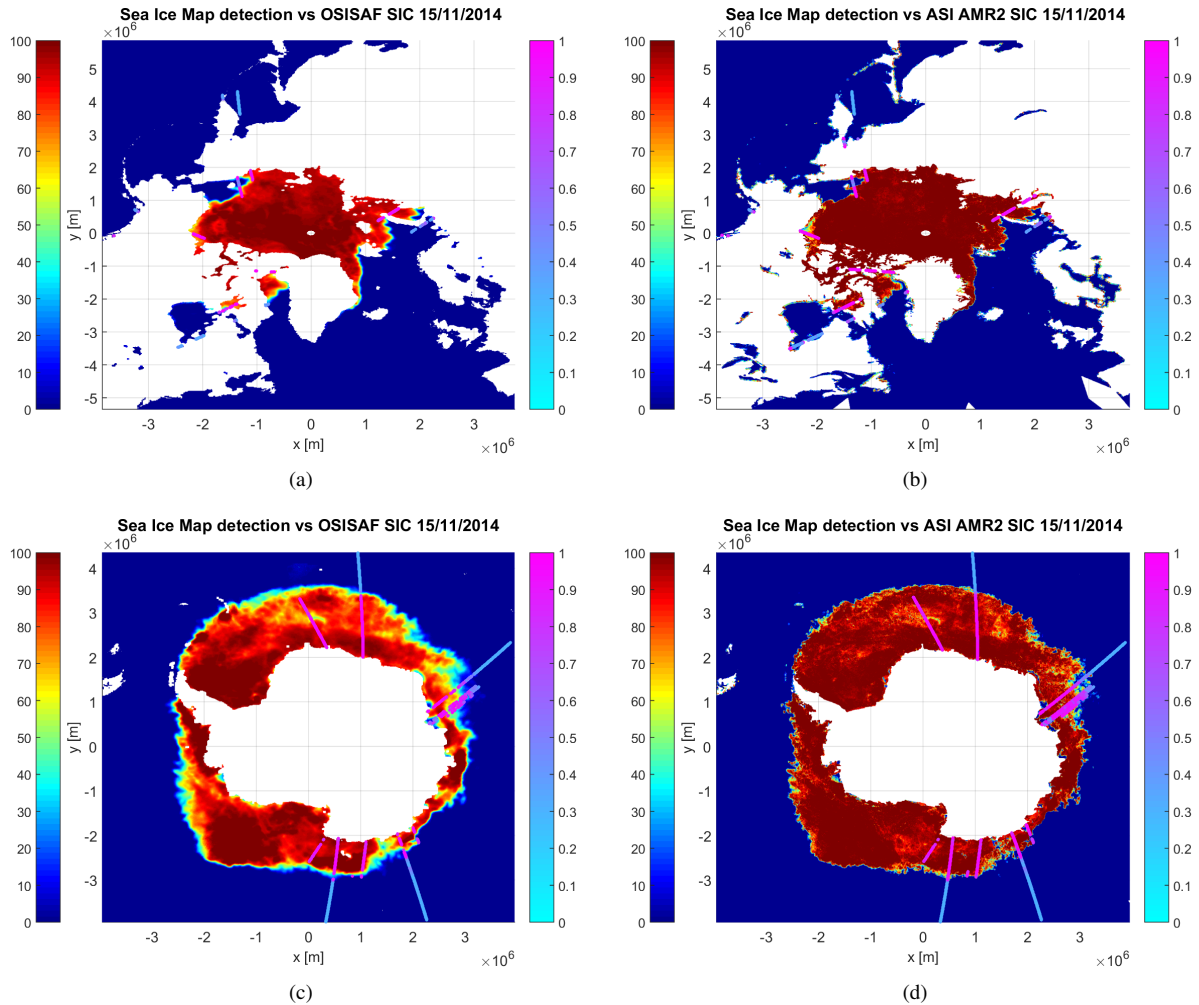

Fig. 3: Sea Ice Concentration Maps of February 20th 2015 from OSISAF and ASI AMSR2 of the northern and Southern hemisphere overlayed with the matched filter GNSS-R approach, (a) Arctic OSISAF, (b) Arctic ASI AMSR2, (c) Antarctic OSISAF, (d) Antarctic ASI AMSR2.

Figure 4 shows a similar image to Fig. 3, but in this case for November 15th 2014. Herein, the Arctic regions are less frozen than in February, as the freezing period has just started, whereas the Antarctic regions have plenty of sea ice as the melting process is just starting. Therein, again the transitions are monitored by the

GNSS-R data. Note that in the Antarctic there is a place close to the coast that has melted before the outer ice layer, and it is detected by the GNSS-R data. Also, note that for those images, there is much less GNSS-R data available. This is because the UK TDS-1 2014 dataset comes from the beginning of the mission whereas the 2015 comes from a more consolidated period of the mission. There is a gap in the GNSS-R data between November 23rd 2014 and January 26th 2015 as there was a Christmas break, and corrupted orbital parameters [39].

Fig. 4: Sea Ice Concentration Maps of November 15th 2014 from OSISAF and ASI AMSR2 of the northern and southern hemisphere overlayed with the matched filter GNSS-R approach, (a) Arctic OSISAF, (b) Arctic ASI AMSR2, (c) Antarctic OSISAF, (d) Antarctic ASI AMSR2.

VI. DISCUSSION

A sea ice detection algorithm has been presented and justified through the sea ice scattering models available in the literature. Several estimators have been proposed to determine the sea ice edge and its performance evaluated through a Bayesian approach. Then, sea ice maps from the different ground-truths available have been shown with the GNSS-R matched filter approach overlaying them. Furthermore, it has been tried to go deeper and determine if the coherent GNSS-R waveform was sensitive to other parameters apart from the sea

ice presence, and therefore it could be used, for instance, for sea ice classification (first year, multi-year, or pure ice [40]). Following the ice scattering coherent model, it would be expected to find the largest power received when there is very low SIC, as the water is freezing and calmed (a property of new ice formation [19]), and water has a very large dielectric constant. When the SIC increases, the equivalent dielectric constant is a mixture of the ice one and water one, and as the dielectric constant of ice is much smaller than the water one, the equivalent dielectric constant decreases, and so the reflected power or the reflected SNR. This brought to the limit means that when the SIC is 100%, the coherent model would work but with a lower echo received. The same reasoning applies to first year ice, whose dielectric constant is larger than multi-year ice, which at the same time its dielectric constant is larger than the pure ice one. Conversely, no correlation was found between the SNR received and the SIC. This might be interpreted as the GNSS-R is not sensitive to the SIC. However, since UK TDS-1 data was not calibrated, and having a mixture of data from different satellites prevents to extract any robust conclusion from the dataset used. This relation should be explored in the future with calibrated data. Also, different roughness scales may apply to this analysis, making more difficult to obtain a clear relation. CYGNSS mission will provide calibrated data, but its orbit, which was selected to monitor tropical cyclones, will prevent from picking reflections from sea ice. In order to test this hypothesis data from the forthcoming European Space Agency (ESA) GNSS rEflectometry, Radio Occultation and Scatterometry (GEROS) mission will be needed. Furthermore, National Aeronautics and Space Administration (NASA) is leading a continuation of the CYGNSS mission and new scientific challenges such as the SIC monitoring could be one of its goals, as the melting of the poles and its consequent rise of the sea level is one of the major problems that concerns the scientific/meteorological community.

Apart from that, herein, we have presented a methodology to detect the presence of sea ice based on the coherency of the scattered signal. When it is coherent, the ground resolution of the GNSS-R data corresponds to the First Fresnel Zone [41], [42], which is approximately 400 m x 400 m meters for a satellite at 650 km altitude. Taking into account the satellite's speed (6 km/s) and 1 second of non-coherent integration, this leads to a final ground-resolution of approximately 6 km x 0.4 km. This resolution is similar to the one achieved by microwave radiometers working at 90 GHz, in the along track direction, and even better in the across-track direction. Furthermore, the spatial resolution of coherent scattered GNSS signals is much better than microwave radiometers working at the same frequency band (L-Band), such as Soil Moisture Ocean Salinity (SMOS), Aquarius, and Soil Moisture Active and Passive (SMAP). This is a major point about this technique, as technology is much cheaper at L-Band than at 90 GHz. Furthermore, L-Band is much less sensitive to atmospheric effects than the 90 GHz frequency band [43], which means that less corrections are required.

One aspect that has not yet been discussed is the Pfa obtained by all the estimators, and the reasons why a false alarm may be produced. The sea ice presence is determined by the coherency of the received signal, which means that the reflected surface must be flat. In several of the datasets used we have realized that close to the sea ice edges the GNSS-R data was detecting ice presence whereas the ground-truth had not yet detected ice. The ground-truth used are SIC maps averaging several images of several radiometer orbits passes, and each pixel data is not time referenced. However, the GNSS-R data it is time referenced. Several continuous data observations showed that when ice was detected close to the ice edges by the GNSS-R technique, but not with the radiometric data, the day after it was detected as an ice pixel by the radiometric data. This indicates that

either the OSISAF data and the AMSR2 data were obtained before the GNSS-R data, or that in the freezing process (new ice generation) the water gets calmed before freezing, and the proposed GNSS-R technique detects ice also when water is calmed.

VII. CONCLUSIONS

This work has presented a methodology to monitor and detect sea ice presence over the Arctic and Antarctic regions using UK TDS-1 GNSS-R data. The detection is based on the analysis of the coherency of the measured DIW or DDM, as when the reflection occurs over an icy region the scattering is mostly coherent whereas when it occurs over open ocean it follows the incoherent model. Three different estimators with different properties are used along the manuscript for the sea ice detection: the normalized DDMA, the TES, and the matched filter approach. Among them, the matched filter approach is preferred as it classifies with only one number between 0 and 1 if it is an ice pixel or an open ocean pixel. Furthermore, it is the one that requires less computational cost and it can be implemented easily on the on-board processing. In order to assess the validity of the algorithms proposed, two different ground-truth datasets have been used: the OSISAF dataset, and the ASI algorithm over AMSR2 data. The best results are obtained for both, the TES in its three versions and the matched filter estimator, over the Arctic region and using the OSISAF dataset as ground-truth, obtaining a Pd of 97% and a Pe of approximately 2.5%.

The relation between the reflected power and the SIC could not be evaluated with the appropriate degree of accuracy as UK TDS-1 GNSS-R data lacks of the measurement of the direct signal, which avoids obtaining calibrated measurements. This means that only relative measurements as the ones performed can be used. However, the encouraging results from this work open the door for future GNSS-R missions, as this GNSS-R technique has the same ground-resolution than microwave radiometers at 90 GHz, being GNSS-R a much more cost-effective technique and less sensitive to atmospheric disturbances. Unfortunately, the CYGNSS mission that will be launched in 2016 will not able to test these algorithms due to its orbit inclination (35°), but other forthcoming GNSS-R missions such as GEROS, or the scientific committee of the CYGNSS follow-on may take into consideration this new application of GNSS-R.

REFERENCES

[1] G. Spreen, L. Kaleschke, and G. Heygster, "Sea ice remote sensing using AMSR-E 89-GHz channels," *Journal of Geophysical Research*, vol. 113, no. C2, p. C02S03, Jan. 2008. [Online]. Available: http://doi.wiley.com/10.1029/2005JC003384

[2] C. Hall and R. Cordey, "Multistatic Scatterometry," in *International Geoscience and Remote Sensing Symposium, 'Remote Sensing: Moving Toward the 21st Century'*. IEEE, 1988, pp. 561–562. [Online]. Available: http://ieeexplore.ieee.org/lpdocs/epic03/wrapper.htm?arnumber=570200

[3] M. Martín-Neira, "A passive reflectometry and interferometry system(PARIS): Application to ocean altimetry," *ESA Journal*, vol. 17, pp. 331–355, 1993. [Online]. Available: http://xenon.colorado.edu/spotlight/kb/gps_reflections/Martin-Neira-PARIS-1993.pdf

[4] M. Martin-Neira, M. Caparrini, J. Font-Rossello, S. Lannelongue, and C. Vallmitjana, "The PARIS concept: an experimental demonstration of sea surface altimetry using GPS reflected signals," *IEEE Transactions on Geoscience and Remote Sensing*, vol. 39, no. 1, pp. 142–150, 2001. [Online]. Available: http://ieeexplore.ieee.org/lpdocs/epic03/wrapper.htm?arnumber=898676

[5] M. Martin-Neira, S. D'Addio, C. Buck, N. Floury, and R. Prieto-Cerdeira, "The PARIS Ocean Altimeter In-Orbit Demonstrator," *IEEE Transactions on Geoscience and Remote Sensing*, vol. 49, no. 6, pp. 2209–2237, Jun. 2011. [Online]. Available: http://ieeexplore.ieee.org/lpdocs/epic03/wrapper.htm?arnumber=5682027

[6] A. Komjathy, J. Maslanik, V. Zavorotny, P. Axelrad, and S. Katzberg, "Sea ice remote sensing using surface reflected GPS signals," in *IGARSS 2000. IEEE 2000 International Geoscience and Remote Sensing Symposium. Taking the Pulse of the Planet: The Role of Remote Sensing in Managing the Environment. Proceedings (Cat. No.00CH37120)*, vol. 7. IEEE, 2000, pp. 2855–2857. [Online]. Available: http://ieeexplore.ieee.org/lpdocs/epic03/wrapper.htm?arnumber=860270

[7] M. Wiehl, B. Legrésy, and R. Dietrich, "Potential of Reflected GNSS Signals for Ice Sheet Remote Sensing," *Progress In Electromagnetics Research*, vol. 40, pp. 177–205, 2003. [Online]. Available: http://www.jpier.org/PIER/pier.php?paper=0210222

[8] S. Gleason, "Remote Sensing of Ocean, Ice and Land Surfaces Using Bistatically Scattered GNSS Signals From Low Earth Orbit," Ph.D. dissertation, University of Surrey, 2006.

[9] ——, "Towards Sea Ice Remote Sensing with Space Detected GPS Signals: Demonstration of Technical Feasibility and Initial Consistency Check Using Low Resolution Sea Ice Information," *Remote Sensing*, vol. 2, no. 8, pp. 2017–2039, Aug. 2010. [Online]. Available: http://www.mdpi.com/2072-4292/2/8/2017/

[10] M. Rivas, J. Maslanik, and P. Axelrad, "Bistatic Scattering of GPS Signals Off Arctic Sea Ice," *IEEE Transactions on Geoscience and Remote Sensing*, vol. 48, no. 3, pp. 1548–1553, Mar. 2010. [Online]. Available: http://ieeexplore.ieee.org/lpdocs/epic03/wrapper.htm?arnumber=5256254

[11] G. Brown, "The average impulse response of a rough surface and its applications," *IEEE Transactions on Antennas and Propagation*, vol. 25, no. 1, pp. 67–74, Jan. 1977. [Online]. Available: http://ieeexplore.ieee.org/lpdocs/epic03/wrapper.htm?arnumber=1141536

[12] C. Rapley and A. P. Cooper, "Applications and Scientific Uses of ERS-1 Radar Altimeter Data," University College London, Tech. Rep., 1985.

[13] M. R. Drinkwater, "K u band airborne radar altimeter observations of marginal sea ice during the 1984 Marginal Ice Zone Experiment," *Journal of Geophysical Research*, vol. 96, no. C3, p. 4555, 1991. [Online]. Available: http://doi.wiley.com/10.1029/90JC01954

[14] P. Woodward, "Radar ambiguity analysis," Tech. Rep., 1967.

[15] V. Zavorotny and A. Voronovich, "Scattering of GPS signals from the ocean with wind remote sensing application," *IEEE Transactions on Geoscience and Remote Sensing*, vol. 38, no. 2, pp. 951–964, Mar. 2000. [Online]. Available: http://ieeexplore.ieee.org/lpdocs/epic03/wrapper.htm?arnumber=841977

[16] T. Elfouhaily, D. Thompson, and L. Linstrom, "Delay-Doppler analysis of bistatically reflected signals from the ocean surface: theory and application," *IEEE Transactions on Geoscience and Remote Sensing*, vol. 40, no. 3, pp. 560–573, Mar. 2002. [Online]. Available: http://ieeexplore.ieee.org/lpdocs/epic03/wrapper.htm?arnumber=1000316

[17] J. Marchan-Hernandez, A. Camps, N. Rodriguez-Alvarez, E. Valencia, X. Bosch-Lluis, and I. Ramos-Perez, "An Efficient Algorithm to the Simulation of Delay–Doppler Maps of Reflected Global Navigation Satellite System Signals," *IEEE Transactions on Geoscience and Remote Sensing*, vol. 47, no. 8, pp. 2733–2740, Aug. 2009. [Online]. Available: http://ieeexplore.ieee.org/lpdocs/epic03/wrapper.htm?arnumber=4813235

[18] D. Pascual, A. Camps, F. Martin, H. Park, A. A. Arroyo, and R. Onrubia, "Precision Bounds in GNSS-R Ocean Altimetry," *IEEE Journal of Selected Topics in Applied Earth Observations and Remote Sensing*, vol. 7, no. 5, pp. 1416–1423, May 2014. [Online]. Available: http://ieeexplore.ieee.org/lpdocs/epic03/wrapper.htm?arnumber=6742726

[19] G. S. Brown, "A theory for near-normal incidence microwave scattering from first-year sea ice," *Radio Science*, vol. 17, no. 1, pp. 233–243, Jan. 1982. [Online]. Available: http://doi.wiley.com/10.1029/RS017i001p00233

[20] V. U. Zavorotny, S. Gleason, E. Cardellach, and A. Camps, "Tutorial on Remote Sensing Using GNSS Bistatic Radar of Opportunity," *IEEE Geoscience and Remote Sensing Magazine*, vol. 2, no. 4, pp. 8–45, 2014. [Online]. Available: http://ieeexplore.ieee.org/lpdocs/epic03/wrapper.htm?arnumber=6985926

[21] P. Beckmann and A. Spizzichino, *The Scattering of Electromagnetic Waves From Rough Surfaces*, artech hou ed.   Artech Print on Demand, 1987.

[22] R. De Roo and F. Ulaby, "Bistatic specular scattering from rough dielectric surfaces," *IEEE Transactions on Antennas and Propagation*, vol. 42, no. 2, pp. 220–231, 1994. [Online]. Available: http://ieeexplore.ieee.org/lpdocs/epic03/wrapper.htm?arnumber=277216

[23] S. Gleason, S. Hodgart, Yiping Sun, C. Gommenginger, S. Mackin, M. Adjrad, and M. Unwin, "Detection and Processing of bistatically reflected GPS signals from low Earth orbit for the purpose of ocean remote sensing," *IEEE Transactions on Geoscience and Remote Sensing*, vol. 43, no. 6, pp. 1229–1241, Jun. 2005. [Online]. Available: http://ieeexplore.ieee.org/lpdocs/epic03/wrapper.htm?arnumber=1433022

[24] A. K. Fung, *Microwave Scattering and Emission Models and their Applications*.   Artech House Publishers, 1994.

[25] ——, "Coherent scattering of a spherical wave from an irregular surface," 1983.

[26] N. Pierdicca, L. Guerriero, R. Giusto, M. Brogioni, and A. Egido, "SAVERS: A Simulator of GNSS Reflections From Bare and Vegetated Soils," *IEEE Transactions on Geoscience and Remote Sensing*, vol. 52, no. 10, pp. 6542–6554, Oct. 2014. [Online]. Available: http://ieeexplore.ieee.org/lpdocs/epic03/wrapper.htm?arnumber=6725659

[27] J. Garrison, A. Komjathy, V. Zavorotny, and S. Katzberg, "Wind speed measurement using forward scattered GPS signals," *IEEE Transactions on Geoscience and Remote Sensing*, vol. 40, no. 1, pp. 50–65, 2002. [Online]. Available: http://ieeexplore.ieee.org/lpdocs/epic03/wrapper.htm?arnumber=981349

[28] E. Cardellach, G. Ruffini, D. Pino, A. Rius, A. Komjathy, and J. L. Garrison, "Mediterranean Balloon Experiment: ocean wind speed sensing from the stratosphere, using GPS reflections," *Remote Sensing of Environment*, vol. 88, no. 3, pp. 351–362, Dec. 2003. [Online]. Available: http://linkinghub.elsevier.com/retrieve/pii/S0034425703001767

[29] A. Komjathy, M. Armatys, D. Masters, P. Axelrad, V. Zavorotny, and S. Katzberg, "Retrieval of Ocean Surface Wind Speed and Wind Direction Using Reflected GPS Signals," *Journal of Atmospheric and Oceanic Technology*, vol. 21, no. 3, pp. 515–526, Mar. 2004. [Online]. Available: http://journals.ametsoc.org/doi/abs/10.1175/1520-0426%282004%29021%3C0515%3AROOSWS%3E2.0.CO%3B2

[30] E. Valencia, A. Camps, X. Bosch-Lluis, N. Rodriguez-Alvarez, I. Ramos-Perez, F. Eugenio, and J. Marcello, "On the Use of GNSS-R Data to Correct L-Band Brightness Temperatures for Sea-State Effects: Results of the ALBATROSS Field Experiments," *IEEE Transactions on Geoscience and Remote Sensing*, vol. 49, no. 9, pp. 3225–3235, Sep. 2011. [Online]. Available: http://ieeexplore.ieee.org/lpdocs/epic03/wrapper.htm?arnumber=5958602

[31] M. P. Clarizia, C. S. Ruf, P. Jales, and C. Gommenginger, "Spaceborne GNSS-R Minimum Variance Wind Speed Estimator," *IEEE Transactions on Geoscience and Remote Sensing*, vol. 52, no. 11, pp. 6829–6843, Nov. 2014. [Online]. Available: http://ieeexplore.ieee.org/lpdocs/epic03/wrapper.htm?arnumber=6744608

[32] V. Zavorotny and A. Voronovich, "Two-scale model and ocean radar Doppler spectra at moderate- and low-grazing angles," *IEEE Transactions on Antennas and Propagation*, vol. 46, no. 1, pp. 84–92, 1998. [Online]. Available: http://ieeexplore.ieee.org/lpdocs/epic03/wrapper.htm?arnumber=655454

[33] F. M. Fetterer, M. R. Drinkwater, K. C. Jezek, S. W. C. Laxon, R. G. Onstott, and L. M. H. Ulander, "Sea ice altimetry," ser. Geophysical Monograph Series, F. D. Carsey, Ed.   Washington, D. C.: American Geophysical Union, 1992, vol. 68, pp. 111–135. [Online]. Available: http://doi.wiley.com/10.1029/GM068 http://doi.wiley.com/10.1029/GM068p0111

[34] S. Andersen, L.-A. Breivik, S. Eastwood, G. Oysten, T. Lavergne, M. Lind, and M. Porcires, "Ocean & Sea Ice SAF: Sea Ice Product User's Manual, OSI-401-a, OSI-402-a, OSI-403-a." Meteo France, Ifremer, EUMETSAT, DMI, Norwegian Meteorological Institute, Tech. Rep., 2014.

[35] "Sea Ice Concentration Maps from AMSR2 data." [Online]. Available: http://www.meereisportal.de

[36] "Ocean & Sea Ice SAF: Sea Ice Concentration Maps." [Online]. Available: http://osisaf.met.no/p/ice/

[37] G. Foti, C. Gommenginger, P. Jales, M. Unwin, A. Shaw, C. Robertson, and J. Roselló, "Spaceborne GNSS reflectometry for ocean winds: First results from the UK TechDemoSat-1 mission," *Geophysical Research Letters*, vol. 42, no. 13, pp. 5435–5441, Jul. 2015. [Online]. Available: http://doi.wiley.com/10.1002/2015GL064204

[38] S. M. Kay, *Fundamentals of Statistical Signal Processing. Volume II: Detection Theory.*, 1st ed. Prentice Hall, 1998.

[39] P. Jales, "TDS-1 GNSS-R data products & access," in *TechDemoSat-1 User Consultation Workshop*, 2015.

[40] F. T. Ulaby, R. K. Moore, and A. K. Fung, *Microwave Remote Sensing: Active and Passive Volume II: Radar Remote Sensing and Surface Scattering and Emission Theory*, 1982, vol. 2.

[41] D. Masters, P. Axelrad, and S. Katzberg, "Initial results of land-reflected GPS bistatic radar measurements in SMEX02," *Remote Sensing of Environment*, vol. 92, no. 4, pp. 507–520, Sep. 2004. [Online]. Available: http://linkinghub.elsevier.com/retrieve/pii/S0034425704001828

[42] S. J. Katzberg, O. Torres, M. S. Grant, and D. Masters, "Utilizing calibrated GPS reflected signals to estimate soil reflectivity and dielectric constant: Results from SMEX02," *Remote Sensing of Environment*, vol. 100, no. 1, pp. 17–28, Jan. 2006. [Online]. Available: http://linkinghub.elsevier.com/retrieve/pii/S0034425705002932

[43] F. T. Ulaby, R. K. Moore, and A. K. Fung, *Microwave remote sensing: Active and passive. Volume 1 - Microwave remote sensing fundamentals and radiometry*, 1981, vol. 1, no. 1.

Alberto Alonso Arroyo (S'11) was born in Barcelona, Spain. He received the M.S. degree in telecommunications engineering in 2011 (BSc+5) and the M.S. in Research on Information and Communication Technologies in 2012 (MSc+2), both from the Universitat Politècnica de Catalunya-BarcelonaTech. He is working toward the PhD degree in GNSS-Reflectometry, with the Passive Remote Sensing Group, Department of Signal Theory and Communications, at the Universitat Politècnica de Catalunya-BarcelonaTech. Currently, he is at National Oceanic and Atmospheric Administration (NOAA) as an invited visiting researcher thanks to a Fulbright grant.
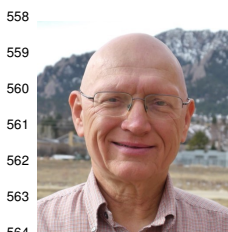
Valery U. Zavorotny Valery Zavorotny (M'01–SM'03-F'10) received the M. S. degree in radio physics from Gorky State University, Gorky, Russia, in 1971, and the Ph.D. degree in physics and mathematics from the Institute of Atmospheric Physics, USSR Academy of Sciences, Moscow, in 1979. Currently he is a Physicist at the Earth System Research Laboratory of the National Oceanic and Atmospheric Administration (NOAA), Boulder, CO. Prior that, he was with the Institute of Atmospheric Physics and Lebedev Physical Institute of the USSR Academy of Sciences, Moscow. Dr. Zavorotny's current research interests are in the areas of modeling of EM wave scattering from rough sea surface, ocean and land remote sensing applications using radar and GNSS reflection techniques. He has more than 150 publications in scientific journals, conference proceedings and book chapters. He is currently a Co-PI, member of Science Team for Cyclone Global Navigation Satellite System (CYGNSS) mission, the project awarded by NASA in 2012 and planned for a launch in October, 2016. Dr. Zavorotny is a member of AGU and a member of Commission F of the U.S. National Committee of URSI. He is a recipient of the Prince Sultan Bin Abdulaziz International Creativity Prize for Water, for development of a new cost-effective technique, GPS Interferometric Reflectometry (GPS-IR), to measure soil moisture, snow depth, and vegetation water content (together with K. Larson, E. Small, and J. Braun).

Adriano Camps (S'91–A'97–M'00–SM'03–F'11) was born in Barcelona, Spain, in 1969. He received the degree in telecommunications engineering and Ph.D. degree in telecommunications engineering from the Universitat Politècnica de Catalunya (UPC), Barcelona, Spain, in 1992 and 1996, respectively. In 1991 to 1992, he was at the ENS des Télécommunications de Bretagne, France, with an Erasmus Fellowship. Since 1993, he has been with the Electromagnetics and Photonics Engineering Group, Department of Signal Theory and Communications, UPC, where he was first Assistant Professor, Associate Professor in 1997, and Full Professor since 2007. In 1999, he was on sabbatical leave at the Microwave Remote Sensing Laboratory, of the University of Massachusetts, Amherst. Since 1993, he has been deeply involved in the European Space Agency SMOS Earth Explorer Mission, and since 2001 on the use of GNSS-R techniques to perform the sea state correction needed to retrieve salinity from radiometric observations. He has received a number of awards for his research and teaching activies, among which the Research Distinction of the Generalitat de Catalunya (2002) for contributions to microwave passive remote sensing; the European Young Investigator Award (2004) of the European Science Foundation, the ICREA Academia award (2009), and the 1st (2000) and 7th (2010) Duran Farell Awards. He has published more than 125 peer-reviewed journal papers, and more than 250 international conference presentations.